ice fluctuations at the type-locality suggest that deglaciation of the three Fremont Lake basin glacial lobes advanced and retreated approximately coevally with most other Rocky Mountain glaciers (*6–8, 27*). Moreover, the deglaciation history of the Fremont Lake basin is in excellent agreement with the corresponding history of portions of the Laurentide Ice Sheet for which ages are well constrained (*28*) and with many marine isotope and ice core records of the last deglaciation (*29*).

REFERENCES AND NOTES

1. E. Blackwelder, *J. Geol.* **23**, 307 (1915).
2. G. M. Richmond, in *Geol. Soc. Am. Centl. Field Guide 201* (1987); *Geologic Map of the Fremont Lake South Quadrangle, Sublette County, Wyoming*, 1:50,000 [*U.S. Geol. Surv. Map GQ-1138* (1973)].
3. M. Stuiver and P. Reimer, *Radiocarbon* **35**, 215 (1993).
4. C. J. Sorenson, *Soils Map of the Fremont Lake South Quadrangle, Sublette County, Wyoming*, 1:24,000 [*U.S. Geol. Surv. Map I-1800* (1987)].
5. P. C. Ives, B. Levin, R. D. Robinson, M. Rubin, *Radiocarbon* **6**, 37 (1964).
6. A. R. Nelson *et al.*, *Geology* **7**, 410 (1979); K. L. Pierce *et al.*, *Geol. Soc. Am. Bull.* **87**, 703 (1976).
7. K. L. Pierce, *U.S. Geol. Surv. Prof. Pap.* **729F**, F1 (1979).
8. S. C. Porter, K. L. Pierce, T. D. Hamilton, in *Late-Quaternary Environments of the United States*, H. E. J. Wright, Ed. (Univ. of Minnesota Press, Minneapolis, 1983), vol. 1, p. 71.
9. S. M. Colman and K. L. Pierce, *Weathering Rinds on Andesitic and Basaltic Stones as a Quaternary Age Indicator, Western United States* (*U.S. Geol. Surv. Publ. 1210*, U.S. Geological Survey, Washington, DC, 1981); S. M. Colman and K. L. Pierce, *Quat. Res.* **25**, 25 (1986).
10. N. C. Sturchio, K. L. Pierce, M. T. Murrell, M. L. Sorey, *Quat. Res.* **41**, 265 (1994).
11. F. M. Phillips *et al.*, *Science* **248**, 1529 (1990); E. T. Brown *et al.*, *Geochim. Cosmochim. Acta* **55**, 2269 (1991).
12. J. C. Gosse, thesis, Lehigh University (1994).
13. ———, E. B. Evenson, J. Klein, B. Lawn, R. Middleton, in preparation.
14. The 3% total analytical uncertainty of ^{10}Be measurements is the reproducibility expected when two completely independent samples are prepared from the same rock. It includes variability during accelerator mass spectrometry analyses, Poisson counting statistics, and any additional variability due to the separation chemistry [C. P. Kohl and K. Nishiizumi, *Geochim. Cosmochim. Acta* **56**, 3583 (1992)]. The total analytical uncertainty has been determined experimentally from studies in the Sierra Nevada (*15*), in Antarctica [R. Giegengack, J. Klein, B. R. Lawn, D. Fink, R. Middleton, *Antarct. J. U.S.* **90**, 14 (1990)], in eastern Pennsylvania [P. Macciaroli, R. Giegengack, J. Klein, R. Middleton, B. Lawn, *Geol. Soc. Am. Abstr. Programs* **26**, A-125 (1994)], and in this study.
15. K. Nishiizumi *et al.*, *J. Geophys. Res.* **94**, 17907 (1989).
16. Splits from samples WY-91-003 and WY-91-035 were completely reanalyzed, yielding concentrations within 0.5% of their mean (5.18×10^5 and 5.13×10^5 atoms per gram and 6.25×10^5 and 6.23×10^5 atoms per gram, respectively).
17. The calibration of (*15*) based on 16 samples, measured on surfaces in the Sierra Nevada with a calibrated radiocarbon age of 11,000 years, gives a production rate of 6.01 ± 0.4 atoms per gram per year at sea level for latitudes >60°. The altitude and latitude factors of D. Lal [*Earth Planet. Sci. Lett.* **104**, 424 (1991)] were used to adjust the production rate to the altitude and latitude of Pinedale (~35 atoms per gram per year). Sources of uncertainty in this calibration applied to Pinedale samples are (i) the assigned age of 11×10^3 years for the glacially striated surfaces [D. H. Clark and A. R. Gillespie, *Geol. Soc. Am. Abstr. Programs* **26**, A-447 (1994)]; (ii) possible variations in the strength of Earth's magnetic field {both a comparison of radiocarbon ages and U-Th ages in coral [E. Bard *et al.*, *Nucl. Instrum. Methods Phys. Res. B* **52**, 461 (1990)] and paleointensity measurements of M. W. McElhinny and W. E. Senanayake [*J. Geomagn. Geoelectr.* **34**, 39 (1982)] suggest that Earth's magnetic field was weaker 10,000 to 20,000 years ago than between 0 and 10,000 years ago, so production rates averaged over the past 20×10^3 years may have been 7% higher than those given in (*15*)}; and (iii) uncertainties in the average geomagnetic latitude of Pinedale introduce an uncertainty of about 10% in the production rate.
18. Ages are reported in units of ^{10}Be years, by analogy with the convention used for radiocarbon dates. This convention recognizes that there may be differences between the calendric time scale and the ^{10}Be time scale because of uncertainties in the production rate of ^{10}Be (*17*).
19. The uncertainty in the age range is the square root of the sum of the squares of the uncertainties of the oldest and youngest dates.
20. We calculated the maximum erosion rate, ϵ_{max} (in millimeters per year), by assuming that the concentration of a cosmogenic nuclide is determined by the rate of erosion and not exposure time; that is, the rate of removal of cosmogenic atoms by erosion is equal to the rate of their production by cosmic rays:

$$\epsilon_{max} \approx 3400/N_{10} \approx 566/T_{eff}$$

where T_{eff} is the apparent age of the sample, $\rho = 2.65$ g cm^{-3}, and N_{10} is the concentration of ^{10}Be (in 10^6 atoms per gram normalized to sea level, high latitude).
21. B. Hallet and J. Putkonen, *Science* **265**, 937 (1994).
22. D. E. Dahms, *Quat. Res.* **42**, 41 (1994); R. D. Hall and R. R. Shroba, *Arct. Alp. Res.* **25**, 368 (1993).
23. If we ignore any underlying older till that may have been overridden, we estimate that the volume of the terminal moraine is at least 25 times that of any individual recessional moraine.
24. W. C. Mahaney, *Géogr. Phys. Quat.* **42**, 337 (1988).
25. On the basis of the relief between Pinedale lateral moraine crests and the Fremont Lake bottom, the valley ice near the northern end of Fremont Lake was at least 610 m thick.
26. A. S. Dyke, *Progr. Phys. Geogr.* **17**, 223 (1993); J. C. Gosse, D. R. Grant, J. Klein, B. Lawn, paper presented at the Canadian Quaternary Association National Meeting, St. John's, Newfoundland (1995).
27. D. R. Butler, *Géogr. Phys. Quat.* **40**, 39 (1986); S. A. Elias *et al.*, *Quat. Res.* **36**, 307 (1991).
28. A. K. Hansel and W. H. Johnson, *Geol. Surv. Sweden Spec. Pap.*, in press; T. V. Lowell, *Geol. Soc. Am. Abstr. Programs* **26**, A-125 (1994).
29. R. B. Alley *et al.*, *Nature* **362**, 527 (1993); S. J. Johnsen *et al.*, *ibid.* **359**, 311 (1992); J. C. Duplessy *et al.*, *ibid.* **320**, 353 (1986); P. U. Clark, *Geol. Soc. Am. Abstr. Programs* **26**, A-255 (1994); *Geology*, in press.

30. We thank J. C. Strasser, P. Baldauf, R. D. Hall, C. D. Harrington, R. Giegengack, and F. Phillips for discussions in the field, suggestions, and reviews. This work was supported by National Science Foundation grants EAR 9206451 and EAR 9208944, Sigma Xi grants GIAR 9201 and 8056, and Geological Society of America grant 4932-92.

21 December 1994; accepted 6 March 1995

Surface Displacement of the 17 May 1993 Eureka Valley, California, Earthquake Observed by SAR Interferometry

Gilles Peltzer and Paul Rosen

Satellite synthetic aperture radar (SAR) interferometry shows that the magnitude 6.1 Eureka Valley earthquake of 17 May 1993 produced an elongated subsidence basin oriented north-northwest, parallel to the trend defined by the aftershock distribution, whereas the source mechanism of the earthquake implies a north-northeast–striking normal fault. The ±3-millimeter accuracy of the radar-observed displacement map over short spatial scales allowed identification of the main surface rupture associated with the event. These observations suggest that the rupture began at depth and propagated diagonally upward and southward on a west-dipping, north-northeast fault plane, reactivating the largest escarpment in the Saline Range.

Measurement of the surface displacement of the Earth caused by a large earthquake is important for understanding its mechanism (*1*). Dense geodetic arrays to monitor surface deformation of the crust can feasibly be set up in only a few areas. In remote regions, SAR interferometry (*2, 3*) can provide high-resolution maps of coseismic surface displacements over broad areas, giving new insights into fault geometry.

We studied the magnitude (*M*) 6.1 Eureka Valley earthquake that occurred on 17 May 1993 on the border between California and Nevada. This earthquake occurred at a depth of 13 km along the west side of the Eureka Valley (*4*) (Fig. 1), one of the westernmost valleys in the wide zone of extension distributed across the Great Basin (*5*). The focal mechanism of the main shock indicates that the earthquake ruptured a north-northeast–striking fault, steeply dipping to the west (*4*). The aftershocks define a north-northwest trend (*6*) and include two shocks of $M \sim 5$ and several of $M > 4$. Small surface ruptures formed in the central part of the Eureka valley (*7*) (arrow A1, Fig. 1).

To map the earthquake displacement, we combined SAR images of the epicentral region acquired by the European remote sens-

Jet Propulsion Laboratory, California Institute of Technology, Pasadena, CA 91109, USA.

ing satellite (ERS-1) before and after the event (8), using the three-pass interferometric method (3, 9). A preseismic interferogram (10) was produced with the use of two images acquired before the event. The phase in the interferogram, once the variation induced by the reference geoid is removed, is proportional to the local topography (Fig. 2, left). The phase in a coseismic interferogram (Fig. 2, center) spanning the seismic event and processed in the same way is the sum of two terms: one proportional to the topography and one proportional to the displacement of the surface related to the earthquake. The phase in the coseismic interferogram is more sensitive to surface displacements than to the topography by several orders of magnitude (3), so centimeter-level displacements contribute substantially to the interferometric fringes in Fig. 2, center (11). The topographic signal can be removed from the coseismic interferogram by scaled difference with the preseismic interferogram (12). The resulting interferogram depicts surface displacements related to the earthquake and aftershocks in a direction parallel to the line of sight to the satellite (Fig. 2, right) (13).

The ring-shaped fringes in the epicentral area of this interferogram (Fig. 2, right) depict subsidence of the surface of the hanging wall in response to the fault slip at depth. The subsidence basin is ~35 km in length and ~20 km in width and is oriented slightly west of north. The fringes appear narrower along the southeast side of the basin than along the west side of it, which is consistent with displacement produced by a west-dipping fault.

A few residual fringes are visible around the depression and in the far field where surface displacements related to the earthquake are unlikely. Most of these fringes are not topographic residuals, because they do not coincide with any features in the preseismic interferogram. The fringes may reflect small surface changes related to water content in the soil or delays in wave propagation through the ionosphere and the troposphere (14).

The northern (AA′) and central (BB′) parts of the subsidence basin are relatively symmetric. This probably results from the great depth of the upper edge of the rupture along these sections of the fault. Some of the surface fractures observed in the Eureka Valley fill basin (arrow A1, Figs. 1 and 3)

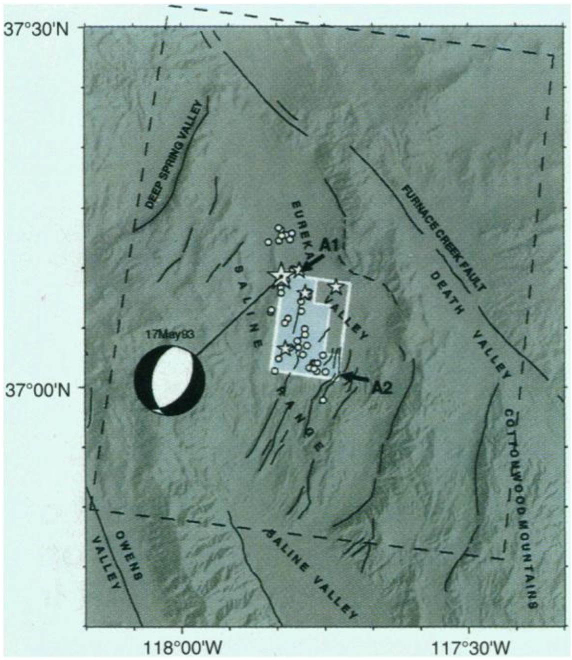

Fig. 1. Active fault map of the Eureka Valley region over a shaded U.S. Geological Survey topographic map. Faults are from interpretation of a Landsat Thematic Mapper image. The white contour depicts the projected fault plane as modeled in this study. The light shaded area in the fault plane is the zone of nonzero slip. Arrow A1 shows the location of surface breaks recognized in the field after the earthquake (7). Arrow A2 points to a fault segment where seismic rupture reached the surface, as inferred from the radar data. Dashed line delineates the area shown in Fig. 2. Large star indicates the location of the main shock; small stars indicate locations of aftershocks of $M > 4.5$; circles indicate smaller aftershocks (6). The focal mechanism of the main shock is depicted (19).

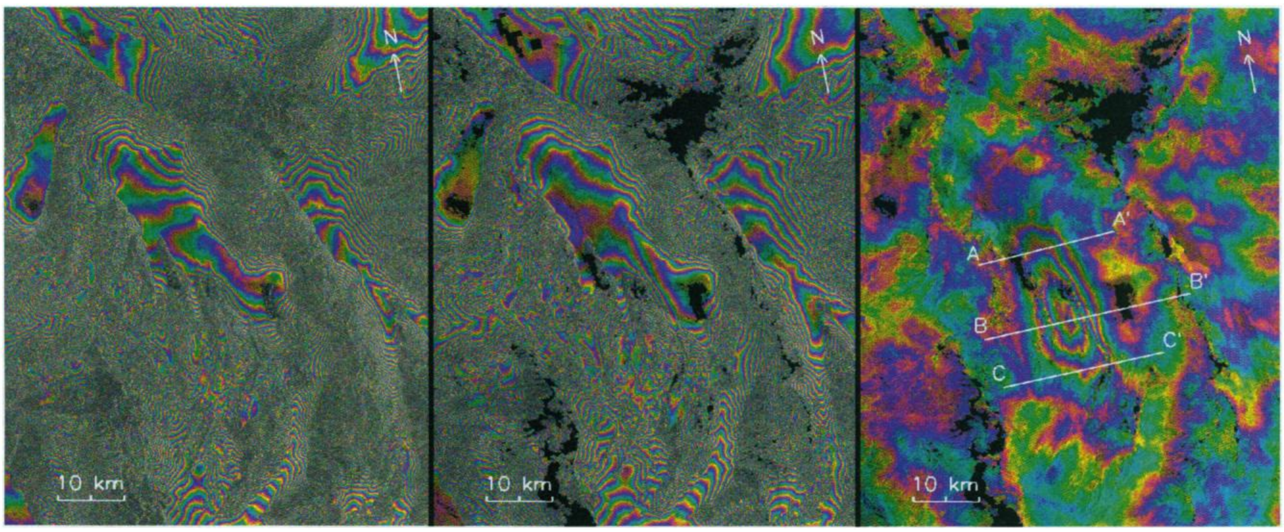

Fig. 2. SAR interferograms formed from combination of the 14 September to 23 November 1992 (**left**) and the 23 November 1992 to 8 November 1993 (**center**) SAR images and by the double difference (**right**) of interferograms shown at left and center. Black areas in center and right panels are zones of low coherence that have been masked before the unwrapping of the phase (12). They correspond to zones of major surface changes, such as sand dunes or cultivated fields, and to zones of phase ambiguities produced by overlays on steep slopes facing toward the satellite. Black masks are absent in left interferogram because it has not been unwrapped. The phase value is color coded and laid over the radar intensity image for reference. The interferometric baseline (11) of the second image pair (center) being smaller than that of the first pair (left), the fringe spacing is larger in the map at left than it is in the center map. At left, a full color cycle corresponds to an elevation difference of 50 m. In the center, a full color cycle can be due to an elevation difference of 78 m, to 28 mm of line-of-sight surface displacement (half the radar wavelength), or to a combination of both. In the three-pass interferogram (right), where the topography has been removed, a full color cycle corresponds to a displacement of the ground of 28 mm in the direction of the satellite. White lines in the right panel indicate location of profiles shown in Fig. 3.

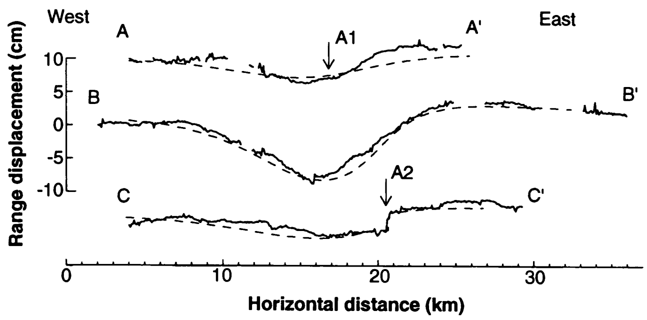

Fig. 3. Profiles of surface displacement observed with the radar (solid lines) and predicted with an elastic dislocation model (dashed lines) (*17*). Profiles are corrected for the geometric distortion induced by topography in radar imagery. Arrow A1 in profile AA′ indicates location where surface cracks were observed (*7*). Arrow A2 in profile CC′ points to the place where the main rupture reached the surface.

showed 5 to 20 mm of vertical separation (*7*). Such offsets are not depicted in the radar measurements, even though the noise in the radar data does not exceed a few millimeters in this area (profile AA′, Fig. 3). A possible explanation is that the fractures were shallow and produced displacements attenuated over a short distance from the surface break. In the averaged radar data, the pixel separation is ~80 m, and local vertical separation of the ground across a small surface break may be undetected. Such fractures could have been generated by shallow aftershocks. Because they lie in the center of the depression and not along its eastern edge, however, it is clear that they do not correspond to the main rupture.

The maximum displacement in the center of the depression is 3.1 cycles of phase, or 8.75 cm in range, corresponding to a vertical displacement of 9.5 cm (*15*). The eastern side of profile BB′ shows a gentle bump, higher than the western side, as a result of the slight uplift of the footwall in response to the down-dip slip on the west-dipping fault.

Along the eastern edge of the southern part of the basin, profile CC′ shows a step of 3 cm. The step can be followed for several kilometers in the interferogram, becoming gradually smoother to the north and south. We interpret this feature as a shallow dislocation along the southern section of the fault and a surface break along a small section of it (*16*). Here the rupture is along an ~100-m-high escarpment in volcanic deposits in the southern Saline Range. The sharpest phase offset is where the escarpment steps 500 m to the right (arrow A2, Figs. 1 and 3).

We conducted a field survey along the fault in order to verify our interpretation. At the base of smaller escarpments (~10 m high) connecting the two main escarpments, we found evidence of surface breaks with vertical displacement of 1 to 3 cm, west side down. The breaks could be followed for a few tens of meters along one escarpment and formed steps between the two major fault scarps. The roughness of the basalt in this area prevented us from making a clear map of the rupture. However, the combination of the radar data and the field observations suggests that the main dislocation reached the surface along the southern segment of the fault. That the surface break was observed along the eastern edge of the subsidence basin is in agreement with a westward dip of the main fault plane at depth.

The fault plane of the main shock strikes north-northeast (*4*), whereas the axis of the subsidence basin and the aftershock distribution are both oriented 5° to 10° west of north (Fig. 1 and Fig. 2, right). This pattern suggests that the slip on the fault plane was along or below a line plunging to the north. Such slip would produce a subsidence basin with a long axis parallel to the trend of the line of maximum slip on the fault plane, rather than to the fault strike direction. If we define this line on a fault plane with dip angle α by the angle δ it makes with the horizontal (Fig. 4), its trend makes an angle $\beta = \tan^{-1}(\cos\alpha \tan\delta)$ with the fault plane strike. An angle β of 15° to 20°, such as that observed in the data, could be obtained with δ = 22° to 29° and a fault plane dipping 50°. The hypocenter of the main shock is at a depth of 13 km, in the northwestern part of the subsidence basin, and the surface rupture is along the southeastern edge of the basin. The rupture thus likely propagated upward and southward on a west-dipping fault plane.

We modeled the earthquake dislocation as a fault plane 15 km long and 16 km wide, striking N7°E and dipping 50° to the west. The plane was divided into 16 patches, and maximum slip was assumed to be distributed near the north-plunging diagonal of the fault. We modeled the slip to be 3 cm at the surface in the south, with no slip on patches located above the zone of maximum slip on the fault plane. The slip values in the lower fault patches were adjusted to match the seismic moment of the earthquake (*4*). An elastic half-space dislocation model (*17*) shows that such fault parameters imply a subsidence basin with a long axis oriented slightly west of north, which is consistent with the radar observations. The predicted displacement along profiles BB′ and CC′ is in good agreement with the displacement observed with the radar (Fig. 3). Along profile AA′, however, the model predicts a smoother

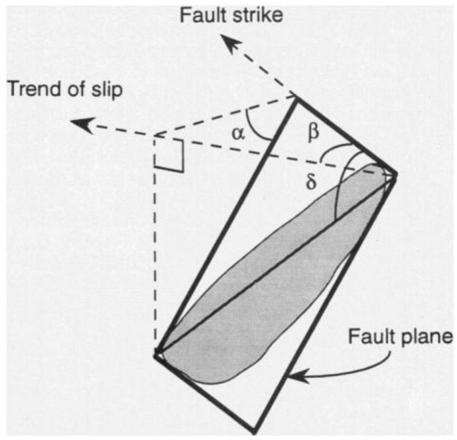

Fig. 4. Sketch showing a plunging slip distribution on a fault plane with dip angle α.

and shallower depression than that observed with the radar. The steep lateral slopes of the observed depression there suggest that shallow sources, such as aftershocks, may have contributed to the subsidence. One of the largest aftershocks actually occurred at shallow depth in this area 2 days after the main event (*18*) (Fig. 1). The effect of this aftershock, which had a steep west-dipping fault, could also explain the angular shape of the interferometric fringe, just north of AA′ (Fig. 2, right). The difference between modeled and observed displacements along AA′ could also be explained by heterogeneities in sediments along the edges of the basin, such as basement scarps connecting with the large surface scarps in the Saline Range.

We have shown that radar interferometry can provide quantitative results regarding the mechanism of an earthquake, even in remote areas where surface ruptures are not apparent. In a region like the Los Angeles basin, where most faults are blind and earthquakes are generally not associated with surface breaks, radar interferometric maps of coseismic displacement would enhance the resolution offered by conventional geodetic techniques and would help determine the geometry of faults at depth.

REFERENCES AND NOTES

1. For example, see C. Tsuboi, *Bull. Earthquake Res. Inst.* **10**, 411 (1933).
2. D. Massonnet *et al.*, *Nature* **364**, 138 (1993).
3. H. A. Zebker, P. A. Rosen, R. M. Goldstein, A. G. Gabriel, C. L. Werner, *J. Geophys. Res.* **99**, 19617 (1994).
4. The Caltech TERRAscope solution is: strike = −172.9°, dip = 47.7° to the west, rake = −109°, depth = 13 km, and moment = 1.6×10^{18} Nm ; the Harvard centroid moment tensor solution is: strike = 218°, dip = 39°, rake = −80°, depth = 15 km, and moment = 1.2×10^{18} Nm. Both mechanisms indicate normal faulting with a mostly down dip motion and a small right lateral component.
5. The region between Owens Valley and Death Valley is characterized by northwest-southeast extension ex-

pressed at the surface in a series of north-northeast prominent normal faults, including the Deep Spring fault, the fault bounding the narrow valley east of the Saline Range, and the fault west of the Cottonwood Mountains (Fig. 1). Within the Saline Range, the deformation is distributed over several smaller faults connecting with Saline Valley across late Cenozoic volcanic deposits. The morphology of these faults, both in the field and on satellite imagery, as well as geodetic measurements suggest recent activity [W. A. Bryant, *Calif. Geol.* **42** (1989); M. Rehis, in *Crustal Evolution of the Great Basin and Sierra Nevada, Field Trip Guide*, M. Lahren, J. Trexler, C. Spinisa, Eds. (University of Nevada, Reno, 1993); J. B. Minster and T. H. Jordan, *J. Geophys. Res.* **92**, 4798 (1987); T. H. Dixon, S. Robaudo, J. Lee, *Tectonics*, in press].

6. In the week after the earthquake, a portable seismic network was deployed in the Eureka Valley by seismologists from the University of Reno, Reno, NV [A. M. Asad, J. N. Louie, S. K. Pullammanappallil, *Eos* **74**, 425 (1994)].
7. The ground ruptures were observed along the base of two west-facing scarps emanating from the Saline Range and extended northward into the valley over a distance of 3 to 4 km. They consisted of left-stepping echelons, generally open fissures, some of them showing a vertical separation of 5 to 20 mm, west side down, which is consistent with the cumulative displacement expressed in the scarps' topography (S. Hecker, personal communication).
8. ERS-1 SAR data were acquired on 14 September 1992, 23 November 1992, and 8 November 1993. Raw SAR data were processed directly to interferograms (*10*).
9. A. G. Gabriel, R. M. Goldstein, H. A. Zebker, *J. Geophys. Res.* **94**, 9183 (1989).
10. In each SAR image pixel, the phase value represents a measure modulo-2π of the distance between the radar antenna and the ground. An interferogram is obtained by averaging the product of one complex SAR image and the complex conjugate of another image, after subpixel coregistration (*3*). The phase of each pixel in an interferogram is the difference of the phase of the corresponding pixels in the two SAR images.
11. The interferometric baseline is the distance between the two orbits from which the data were acquired. In an interferogram, the ambiguity height is defined as the topographic elevation difference that would produce a phase variation of 2π and is inversely proportional to the component of the baseline that is perpendicular to the satellite line of sight. In the coseismic interferogram, the ambiguity height is about 78 m and varies by 7% across the scene. On the other hand, the line-of-sight surface displacement that would produce a phase variation of 2π is 28 mm (half the radar wavelength), independent of the imaging geometry. Therefore, the sensitivity to surface displacement is about 2785 times greater than to elevation variations.
12. Differencing the phase of two interferograms requires one phase field to be scaled to the same fringe rate as the other (*3*), so at least one phase field must be unwrapped [R. M. Goldstein, H. A. Zebker, C.L. Werner, *Radio Sci.* **23**, 713 (1988)]. The ability to unwrap the phase depends on the noise level in the system and the fringe rates in the image. Because the coseismic interferogram in Fig. 2, center, has a smaller fringe rate than that in Fig. 2, left, we unwrapped the coseismic phase, scaled it to the intrinsic fringe rate of the preseismic interferogram, and computed their difference. We then unwrapped the resulting interferogram, which has many fewer fringes, and scaled the phase back to the coseismic rate (Fig. 2, right).
13. For ERS-1, the satellite line of sight is nearly perpendicular to the orbit and has an incidence angle of 23° in the center of the scene [European Space Agency, *ERS-1 System* (ESA Publications Division, ESTEC, Noordwijk, Netherlands, 1992)].
14. Atmospheric phase propagation delays estimated for L-band microwaves by the Global Positioning System can reach about 2 m through the ionospheric and tropospheric layers [D. M. Tralli and S. M. Lichten, *Bull. Geod.* **64**, 127 (1990)]. SAR interferograms probably depict variations of this signal across a scene, but the distinction from effects due to other sources is unclear.
15. In the middle of the depression, the displacement of the ground is essentially vertical, so its magnitude is given by the observed value of the range displacement divided by the cosine of the incidence angle (*13*).
16. A phase offset of 2.8 cm could arise from a phase-unwrapping error, which is most likely to occur in regions of sharp topography such as that of the Saline Range. However, when following a close contour, a phase-unwrapping error must be balanced by a phase offset of opposite sign. The fact that it is possible to connect both ends of profile CC′, following a smooth phase contour running around the zone of phase discontinuity, allows us to rule out this hypothesis.
17. Y. Okada, *Bull. Seismol. Soc. Am.* **75**, 1135 (1985).
18. The aftershock sequence includes four events of $M > 4.5$ (Fig. 1). One of them occurred near the northeast part of the subsidence basin and has the following parameters: strike = −179.3°, dip = 74° to the west, rake = −101°, depth = 5 km, and moment = 1.23×10^{16} Nm (*19*).
19. H. K. Thio and H. Kanamori, *Bull. Seismol. Soc. Am.*, in press.
20. We thank S. Hecker for providing an unpublished surface rupture map, J. Louie for providing relocated aftershock coordinates, R. Armijo for participation in field work, and E. Ivins and K. Hudnut for critically reading the first version of the manuscript. ERS-1 data were provided by the European Space Agency. The work was done at the Jet Propulsion Laboratory, California Institute of Technology, under contract with NASA.

9 December 1994; accepted 8 February 1995

Inactivation of the Type II TGF-β Receptor in Colon Cancer Cells with Microsatellite Instability

Sanford Markowitz,* Jing Wang,† Lois Myeroff,† Ramon Parsons,† LuZhe Sun, James Lutterbaugh, Robert S. Fan, Elizabeth Zborowska, Kenneth W. Kinzler, Bert Vogelstein, Michael Brattain, James K. V. Willson

Transforming growth factor–β (TGF-β) is a potent inhibitor of epithelial cell growth. Human colon cancer cell lines with high rates of microsatellite instability were found to harbor mutations in the type II TGF-β receptor (RII) gene. Eight such examples, due to three different mutations, were identified. The mutations were clustered within small repeated sequences in the RII gene, were accompanied by the absence of cell surface RII receptors, and were usually associated with small amounts of RII transcript. RII mutation, by inducing the escape of cells from TGF-β–mediated growth control, links DNA repair defects with a specific pathway of tumor progression.

TGF-β inhibits the growth of multiple epithelial cell types, and loss of this negative regulation is thought to contribute to tumor development (*1–5*). Studies have shown that TGF-β suppresses the growth of certain cancer cell lines, that antisense inhibition of TGF-β enhances the tumorigenicity of weakly tumorigenic cancer cell lines, and that certain tumor cells can become unresponsive to TGF-β (*2–5*). The TGF-β growth inhibitory signal is transduced through two receptors, type I (RI) and type II (RII), which function as a heteromeric complex (*6, 7*). We investigated whether inactivation of TGF-β receptors is a mechanism by which human colon cancer cells lose responsiveness to TGF-β. We found that RII receptors were inactivated in a subset of colon cancer cell lines. RII inactivation was common in tumor cells exhibiting microsatellite instability (hereafter referred to as RER^+, for "replication errors"), but not in RER^- cells (*8*).

We initially examined the expression of RI and RII transcripts in 38 human colon tumor cell lines using a ribonuclease (RNase) protection assay. RI transcripts were detected in all samples, whereas RII transcripts were undetectable or present at markedly reduced amounts in 12 (32%) of the samples (Fig. 1, A and B). For unrelated purposes, we had independently assayed these cell lines for the RER phenotype. Nine of 11 RER^+ but only 3 of 27 RER^- cell lines showed reduced RII expression (Fig. 1B) (*9–11*). This correlation was highly significant [probability (*P*) <0.001 by χ^2 test]. Southern (DNA) blot analysis indicated that loss of the RII transcript in the RER^+ cells was unlikely to be due to deletions or rearrangements of the RII gene (*12*).

To show that RII inactivation in the RER^+ cells was not simply a trait selected for during cell culture, we examined RII expression in tumor xenografts that had been de-

S. Markowitz, L. Myeroff, J. Lutterbaugh, E. Zborowska, J. K. V. Willson, Department of Medicine and Ireland Cancer Center, University Hospitals of Cleveland and Case Western Reserve University, Room 200, 11001 Cedar Road, Cleveland, OH 44106, USA.
J. Wang, L.-Z. Sun, R. S. Fan, M. Brattain, Department of Biochemistry and Molecular Biology, Medical College of Ohio, Toledo, OH 43699, USA.
R. Parsons and K. W. Kinzler, Johns Hopkins University Oncology Center, 424 North Bond Street, Baltimore, MD 21231, USA.
B. Vogelstein, Howard Hughes Medical Institute, 4000 Jones Bridge Road, Chevy Chase, MD 20815, USA, and Johns Hopkins University Oncology Center, 424 North Bond Street, Baltimore, MD 21231, USA.

*To whom correspondence should be addressed.
†These authors contributed equally to this work.